Comput Mech (2006) 37: 408–425
DOI 10.1007/s00466-005-0713-2

ORIGINAL PAPER

B. A. Younis · V. P. Przulj

# Computation of turbulent vortex shedding

Received: 18 February 2005 / Accepted: 9 May 2005 / Published online: 10 August 2005


**Abstract** The paper reports on the prediction of the flow field around smooth cylinders in cross flow at high Reynolds number. Both circular and square-sectioned cylinders are considered. The principal feature of these flows, and the primary cause for the difficulty in their prediction, is the development of a von Karman vortex street leading to significant fluctuations in surface pressures. It has already been established from several previous studies that eddy-viscosity closures fail to capture the correct magnitude of these fluctuations though there is no consensus as to the underlying causes. In this work, it is argued that the organized fluctuations in the mean-flow field introduce energy into the random turbulence motions at a frequency that corresponds exactly to the shedding frequency and that, as a consequence, it becomes necessary to explicitly account in the turbulence closure for the resulting modification of the spectral transfer process. A proposal to account for this direct energy transfer in the context of two-equation eddy-viscosity closures is put forward and is checked by comparisons with experimental data from both square and circular cylinders at high Reynolds number. Uncertainties in the predictions due to numerical discretization errors are systematically minimized. The outcome of comparisons with experimental data and with results from alternative closures, including Large-Eddy Simulations, validate the proposal.

**Keywords** Turbulent vortex shedding · Turbulence closures · Unsteady RANS

**Nomenclature**

| | |
|---|---|
| $B_f$ | Blockage ratio |
| $C_D$ | Drag coefficient ($= F_D/\frac{1}{2}\rho U_o^2 L^2$) |
| $C_L$ | Lift coefficient ($= F_L/\frac{1}{2}\rho U_o^2 L^2$) |
| $C_p$ | Wall static pressure coefficient ($= (p - p_o)/\frac{1}{2}\rho U_o^2$) |
| $D$ | Cylinder diameter |
| $F_D$ | In-line component of total force |
| $F_L$ | Transverse component of total force |
| $f$ | Frequency of vortex shedding |
| $H$ | Cylinder height |
| $T_u$ | Relative turbulence intensity |
| $k$ | Turbulence kinetic energy |
| $k_f$ | Kinetic energy of total (periodic + turbulent) fluctuations per unit mass |
| $L$ | Characteristic length (D for circular cylinder, H for square cylinder) |
| $\overline{L_r}$ | Length of recirculation zone |
| $p$ | Time-averaged pressure |
| $Q$ | Mean-flow kinetic energy($= \frac{1}{2} U_i U_i$) |
| $Re$ | Reynolds number ($= \rho\ U_o\ L/\mu$) |
| $St$ | Strouhal number ($= f\ L/U_o$) |
| $t^*$ | Dimensionless time ($=\ U_o\ t/L$) |
| $U_i$ | Time-averaged velocity components |
| $u_i$ | Fluctuating velocity components |
| $\overline{u_i u_j}$ | Reynolds-stress tensor |
| $x_i$ | Coordinate directions |
| $Y^+$ | Normal distance in wall coordinates |

**Greek symbols**

| | |
|---|---|
| $\Delta t^*$ | Non-dimensional time-step ($=\ \Delta t U_o/L$) |
| $\Delta n_c$ | Distance from cell center to wall |
| $\epsilon$ | Rate of dissipation of k |
| $\rho$ | Fluid density |
| $\kappa$ | von Karman constant |
| $v$ | Kinematic viscosity |

B. A. Younis (✉)
Department of Civil and Environmental Engineering,
University of California Davis,
CA 95616, USA
E-mail: bayounis@ucdavis.edu

V. P. Przulj
Ricardo Software, Shoreham-by-sea,
West Sussex, BN43 5FG, UK

$\mu$ Dynamic viscosity
$\sigma$ Prandtl number

**Subscripts**
$w$ Wall
$o$ Inlet
$t$ Turbulent

## 1 Introduction

The prediction of vortex shedding from smooth cylinders continues to receive much attention due to the frequent occurrence of such flows in nature and in engineering practice [1], [2]. From an engineering perspective, the safe and economic design of such diverse structures as towers, masts, chimneys, bridge piers and offshore platforms requires a practical and reliable predictions method for estimating the magnitudes and frequency of the in-line and transverse forces associated with the shedding of vortices from these structures. The requirements in such a method are two fold. Firstly, the method should yield results that are of reasonable engineering accuracy for a wide range of geometries and flow parameters. These parameters often combine to yield very high values of the Reynolds number which makes more difficult the task of obtaining numerically-accurate simulations. Secondly, the method should be practical in the sense of being robust when used for complex geometries and in being affordable in terms of computing resources. Specifically, and to be of use for routine engineering analysis, the method must be capable of producing results in reasonable turn-around times. At present, this requirement rules out Large–Eddy Simulations (LES) as the tool of choice for such applications. While enormous progress in understanding the physics of unsteady separated flows at low Reynolds number has been achieved using this technique ([3], [4]), its use as a tool for engineering predictions has been limited by the prohibitive costs inherent in the need to employ very fine meshes and small time-step sizes to resolve a significant portion of the turbulence energy spectrum [5]. Turbulence closures are still generally considered to be the practical approach for the solution of problems of engineering interest but there remains a great deal of uncertainty regarding their suitability in flows where vortex shedding occurs. Franke and Rodi [6], for example, reported that the use of log–law assumptions to provide wall boundary conditions lead to damping of the unsteady flow field around a square cylinder with the result that vortex shedding was ultimately suppressed and a steady–state solution obtained instead. Similarly, Celik and Shaffer [7] reported poor agreement with circular cylinder data when using a conventional turbulence closure. Medic [8], on the other hand, found that shortcomings in the prediction of vortex shedding that have previously been attributed to the turbulence closure have their origins in the use of dissipative discretization schemes leading to numerical diffusion errors that are sufficiently large as to suppress the shedding process. What is not in doubt, however, is that turbulence closures (as characterized by the widely-used $k$-$\epsilon$ model) fail, in their standard form, to capture the correct level of fluctuations in the pressure field associated with the vortex shedding ([9], [10]). Several alternative reasons for this result have been put forward, and proposals made for improvements. Kato and Launder [11], for example, attributed the defect to the generation of high levels of turbulence kinetic energy at the stagnation point ahead of a square cylinder and found that improvements can be obtained by reducing the normal-strain contribution to the rate at which this quantity is generated there. Application of the same model to the circular cylinder produced even poorer agreement with experiment than the standard model [12]. In none of the proposals was allowance made for the effects of the interactions between the large-scale *organized* periodicity of the mean flow and the *random*, small-scale high-frequency motions that characterize turbulence. The purpose of this paper is to introduce a turbulence closure that explicitly accounts for these interactions and to put on record its performance in relation to data from both square and circular cylinders. The mathematical basis of the study is presented in the next section. Computational details are presented in Sect. 3 followed by presentation and discussion of the results. A summary of the main findings is given in Sect. 5. Issues related to numerical uncertainty are considered in the Appendix.

## 2 Mathematical formulation

### 2.1 Mean-flow equations

The flows considered are governed by the incompressible, unsteady forms of the equations for conservation of mass and momentum. As is customary in practical approaches to modeling of turbulent flows, the variables in the instantaneous equations are averaged over a time interval $\Delta t$:

$$\phi = \frac{1}{\Delta t}\int_{t}^{t+\Delta t} \hat{\phi}\ \mathrm{d}t \tag{1}$$

where $\phi$ and $\hat{\phi}$ signify, respectively, the averaged and instantaneous values of a general variable.

The choice of $\Delta t$ depends on the nature of the flow considered. In statistically-stationary flows, the conventional Reynolds averaging would be appropriate with $\Delta t \to \infty$. For the present flows, $\Delta t$ can be taken to be equivalent to the computational time-step size. This would mean that all motions with time scales smaller than the computational time step would not be captured in the computations and their effects must be accounted

for via a turbulence closure. This would also mean that motions with larger time scales are captured directly. Conceptually, this approach to averaging the governing equations is quite different from the more usual ensemble (or phase) averaging which would require the period of oscillations to be known *a priori*. In practice, however, the precise interpretation placed on the averaging process is quite immaterial as the final outcome is the same; namely, time-averaged equations which, using conventional Cartesian tensor notation, are written as:

$$\frac{\partial U_i}{\partial x_i} = 0, \tag{2}$$

$$\frac{\partial U_i}{\partial t} + U_j \frac{\partial U_i}{\partial x_j} = \frac{\partial}{\partial x_j}\left(\nu \frac{\partial U_i}{\partial x_j} - \overline{u_i u_j}\right) - \frac{1}{\rho}\frac{\partial p}{\partial x_i}. \tag{3}$$

## 2.2 Turbulence closure

The unknown correlations in Eq. (3) are obtained here from Boussinesq's linear stress-strain relationship:

$$-\overline{u_i u_j} = \nu_t\left(\frac{\partial U_i}{\partial x_j} + \frac{\partial U_j}{\partial x_i}\right) - \frac{2}{3}\delta_{ij}k. \tag{4}$$

In the $k$-$\epsilon$ model, the kinematic eddy viscosity is computed from:

$$\nu_t = C_\mu \frac{k^2}{\epsilon} \tag{5}$$

with $k$ and $\epsilon$ obtained from the solution of the equations:

$$\frac{\partial k}{\partial t} + U_j \frac{\partial k}{\partial x_j} = \frac{\partial}{\partial x_j}\left(\left(\nu + \frac{\nu_t}{\sigma_k}\right)\frac{\partial k}{\partial x_j}\right) + P_k - \epsilon \tag{6}$$

$$\frac{\partial \epsilon}{\partial t} + U_j \frac{\partial \epsilon}{\partial x_j} = \frac{\partial}{\partial x_j}\left(\left(\nu + \frac{\nu_t}{\sigma_\epsilon}\right)\frac{\partial \epsilon}{\partial x_j}\right) + C_{\epsilon 1}\frac{\epsilon}{k}P_k - C_{\epsilon 2}\frac{\epsilon^2}{k} \tag{7}$$

In the above, $P_k$ is the rate of production of turbulence kinetic energy:

$$P_k = -\overline{u_i u_j}\frac{\partial U_i}{\partial x_j} \tag{8}$$

The $k$-$\epsilon$ model was developed with reference to data from statistically-stationary flows and the various coefficients that appear in its formulation were calibrated using data from wall-bounded and free shear flows in approximate local equilibrium [13]. It has already been mentioned that this model fails badly in the prediction of flows dominated by vortex shedding in that it predicts a far weaker vortex shedding intensity than that observed in measurements. We take the view that the establishment of a vortex shedding field in a turbulent flow leads to direct energy input from the periodic mean-flow oscillations into the random turbulence motions. This direct energy supply occurs at a frequency that corresponds exactly to the vortex-shedding frequency. This view is supported by results from a number of experiments including, for example, the measurements of Durao et al. [14] of the turbulence energy spectrum in the unsteady wake behind a square cylinder and the measurements of Jung and Park [15] in the wake of an airfoil. Now a fundamental assumption in turbulence closures developed with reference to statistically-stationary flows is that of spectral equilibrium. This requires the rate of dissipation of turbulence kinetic energy by the action of viscosity on the small scales (i.e., $\epsilon$) to respond directly to changes in the rate of energy input at the large scales due to the working of the turbulent stresses against the mean rates of strain (Eq. 8). The presence of a direct input of energy at a discrete frequency negates this assumption. The immediate implication is that, in periodic flows, the dissipation-rate equation should be modified in such a way as to reflect the expected enhancement of this parameter due to vortex shedding. The proper way for accounting for the effects of mean-flow periodicity on the energy-transfer process is to re-define the rate of production term (Eq. 8) to allow for the increase in $k$ due to the direct energy input from the mean-flow periodicity. This additional contribution will then appear in the 'production-of-dissipation' term in the $\epsilon$ equation where its effect will be to felt mainly through enhancement of the levels of this parameter relative to a statistically-stationary case. The same effect can be achieved, albeit indirectly, through the dissipation rate equation only [9]. Guidance on how this may be achieved was provided in [16] by consideration of an idealized distorted energy spectrum. Thus if $E(\kappa)$ is the energy spectrum function, its form in the energy-production range in statistically-stationary flows can be taken as [17]:

$$E(\kappa) = A^0 \kappa^s \tag{9}$$

where $A^0$ is a constant and $\kappa$ is the wavenumber vector. The index $s$ is a matching index whose precise value is immaterial to the present discussion. When vortex shedding is present, the shape of the distorted spectrum now varies in time and may be approximated as:

$$E(\kappa, t) = (A^0 + A^1(t))\kappa^s \tag{10}$$

where $A^1(t)$ must vanish in the steady limit. The turbulence kinetic energy $k$ is related to $E(\kappa, t)$ via [18]:

$$k = \int_0^\infty E(\kappa, t)\mathrm{d}\kappa, \tag{11}$$

and

$$\frac{\mathrm{d}k}{\mathrm{d}t} = -\epsilon \tag{12}$$

By postulating a shape for $E(\kappa, t)$ based on the measured spectrum, and after integration of Eq. 11 there results:

$$k = 3s + \frac{5}{2}(s+1)A(t)\kappa_m^{s+1}. \tag{13}$$

**Table 1** Coefficients of turbulence closures

| Model | $C_\mu$ | $\sigma_k$ | $\sigma_\epsilon$ | $C_{\epsilon 1}$ | $C_{\epsilon 2}$ | $C_t$ | $\beta$ | $\eta_o$ |
|---|---|---|---|---|---|---|---|---|
| Modified | 0.09 | 1.0 | 1.30 | 1.44 | 1.92 | 0.38 | — | — |
| RNG | 0.0845 | 0.72 | 0.72 | 1.42 | 1.68 | — | 0.012 | 4.38 |

where $\kappa_m$ is the wavenumber which corresponds to the location of the vortex-shedding frequency. Now by differentiating Eq. 13 twice, an equation for the rate of change of dissipation with time is obtained:

$$\frac{\mathrm{d}\epsilon}{\mathrm{d}t} = -C_{\epsilon 2}\frac{\epsilon^2}{k} - \frac{1}{s+1}\frac{\epsilon}{A^t}\frac{\mathrm{d}A^t}{\mathrm{d}t}, \tag{14}$$

Note the emergence of an additional source of dissipation which is finite only in statistically non-stationary flows and whose precise form will obviously depend on the assumed form for $A^1(t)$. The most straightforward way to introduce this additional term into the dissipation rate equation is to redefine the coefficient $C_{\epsilon 1}$ thus:

$$C^*_{\epsilon 1} = C_{\epsilon 1}\left(1 + C_t\frac{k}{\epsilon}\frac{1}{Q+k}\left|\frac{\partial(Q+k)}{\partial t}\right|\right) \tag{15}$$

where $Q$ is the mean-flow kinetic energy per unit mass. Notice the use of the modulus of the derivative of the total kinetic energy in recognition of the fact that the observed peak in the energy spectrum remains in place at all phases of the shedding cycle. The modification

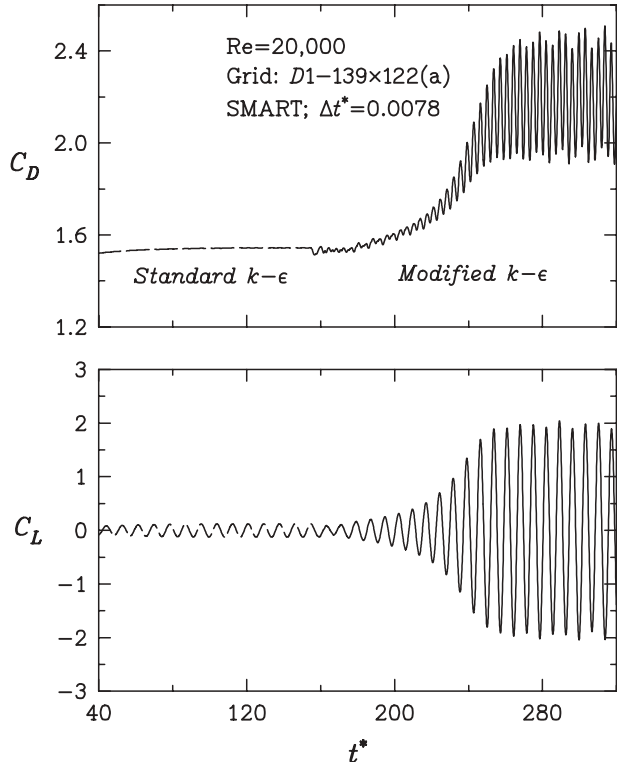


**Fig. 1** Square cylinder (Re = 20,000). Predicted $C_D$ and $C_L$ before and after the unsteady modification

involves a coefficient $C_t$ whose value (Table 1) was arrived at by numerical optimization [19]. The designation "modified" will henceforth be used to indicate that the predictions were obtained with the use of Eq. (15). A demonstration of the need for this modification can be seen from Fig. 1 which shows the computed lift and drag coefficients for a square cylinder at Re = 20,000. Results with the $k$-$\epsilon$ model with and without the modification of Eq. (15) are plotted and these clearly show the amplification in the shedding intensity associated with the proposed modification. Further discussion of these results follows later in this paper.

The requirement to improve on the performance of standard eddy-viscosity models in flows that are far removed from equilibrium has motivated the development of an alternative adaptation to the $k$-$\epsilon$ model; namely the Renormalization Group (RNG) model of Yakhot et al. ([20]). This model differs from the parent model in two respects: the coefficients are assigned somewhat different values but, more importantly, the $\epsilon$ equation now has an additional source term (R) which brings into this equation a strong dependence on the ratio of the turbulence time scale ($k/\epsilon$), which is representative of the rate of transfer of energy across the spectrum, to the mean-flow time scale, the quantity most strongly modified in the presence of vortex shedding. This additional source term is defined as:

$$\begin{aligned} R &= \frac{C_\mu\eta^3(1-\eta/\eta_o)}{1+\beta\eta^3}\frac{\epsilon^2}{k} \\ \eta &= S\frac{k}{\epsilon} \\ S &= \sqrt{\frac{1}{2}\left(\frac{\partial U_i}{\partial x_j}+\frac{\partial U_j}{\partial x_i}\right)^2} \end{aligned} \tag{16}$$

Because of this dependence on the time-scales ratio, it is likely that the RNG model will also yield improvements in the prediction of the present flows. Therefore, predictions will be obtained with this model as well, both to put on record its performance and, also, to provide a base for the assessment of the present proposal.

The coefficients that appear in the present, modified, model and in the RNG formulation are assigned their standard values which are listed in Table 1.

## 3 Computational method

The governing equations were solved using the finite-volume methodology described in [21]. Equations (3)–(7) were integrated, term-by-term, over irregular cells formed from non-orthogonal meshes. Gauss's divergence theorem was used to relate the volume integrals to surface integrals so that the integrated form of the conservation equation for the general variable $\phi$ takes the form:

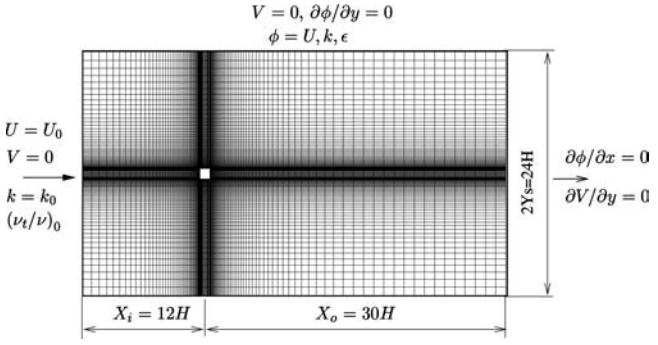


**Fig. 2** Square cylinder. Grid $D1$ and domain boundaries

$$\frac{\mathrm{d}}{\mathrm{d}t}\int_V \rho\phi \,\mathrm{d}V + \oint_A \rho\phi U_k n_k \mathrm{d}A = \oint_A \Gamma_\phi \frac{\partial\phi}{\partial x_k}\, n_k \,\mathrm{d}A + \int_V s_\phi^V \,\mathrm{d}V + \oint_A s_\phi^A \, n_k \,\mathrm{d}A \tag{17}$$

where $n_k$ is the outward unit normal vector. The convective and diffusive fluxes across the cell faces were evaluated using by a number of alternative second– and third–order accurate schemes. These included the SMART [22] and the QUICK [23] schemes. The resulting algebraic equations were solved using Stone's Strongly Implicit Procedure which is based on incomplete lower-upper decomposition. The SIMPLE algorithm [24] was used to couple the solution of the continuity and momentum equations. At each new time step, the mean-flow and turbulence-model equations were solved iteratively till the sum of the normalized residuals for all variables fell below $10^{-6}$. No underrelaxation was used, with typically 3–5 outer iterations being required to satisfy the prescribed convergence criterion. The requirements for numerical accuracy are particularly severe for unsteady separated flows at high Reynolds number. A summary of the tests performed to quantify the numerical uncertainty in the computed results is presented in the Appendix.

### 3.1 Solution domain and grids

Figure 2 shows the computational grid used for the square-cylinder simulations and defines the extent of the solution domain in terms of the cylinder's height, $H$. The dimensions shown were arrived at as a result of the tests reported in the Appendix. The grid shown (hereafter denoted as $D1$) consists of a total of $139 \times 122$ cells, non-uniformly distributed. The grid lines were concentrated near the cylinder walls with 24 cells being in contact with each side. The normalized distance from the cell center to the wall ($\Delta n_c/H$) was 0.014. The grid lines were expanded away from the cylinder with an expansion ratio of 7.5 % in each direction. The blockage ratio (ratio of cylinder width to domain width at inlet) produced by using the above solution domain was $B_f = 4.17\%$. This is approximately equal to the values obtained in the experiments of Lee [25] and Bearman and Obasaju [26] but is smaller than that in the experiments of Lyn [27]. Computations were performed on several other grids, as is detailed in the Appendix. Of those, grid $D2$ is of particular interest since it too contains 24 nodes per side but with the blockage ratio of 8.33%. The results obtained with this grid will help quantify the sensitivity of the computations to the blockage ratio. The main parameters of some of the grids used are given in Table 2. Computations of the flow around the circular cylinder were performed for several values of Reynolds number. A representative grid, used to compute the flow at $\mathrm{Re} = 1.4 \times 10^5$, is shown in Fig. 3.

**Table 2** Square cylinders. Parameters of numerical grids used

| Grid [NI×NJ] | $X_i/H$ | $X_o/H$ | $Y_s/H$ | $f_{ex}$ | $f_{ey}$ | $\Delta n_c/H$ | $\%B_f$ |
|---|---|---|---|---|---|---|---|
| $D0 - 106 \times 108$ | 12 | 30 | 12 | 1.10 | 1.10 | 0.02 | 4.17 |
| $D1 - 139 \times 122(a)$ | 12 | 30 | 12 | 1.075 | 1.075 | 0.014 | 4.17 |
| $D1 - 139 \times 122(b)$ | 12 | 30 | 12 | 1.0635 | 1.062 | 0.02 | 4.17 |
| $D2 - 114 \times 92$ | 5.5 | 29.5 | 6 | 1.076 | 1.076 | 0.02 | 8.33 |

### 3.2 Boundary and initial conditions

The boundary conditions used here are shown in Fig. 2 for the square-cylinder flows. Similar conditions were applied for the circular cylinders. At inlet, uniform profiles of streamwise velocity, $k$ and $\epsilon$ were prescribed. The measurements of Lee [25] and Gartshore [28] for

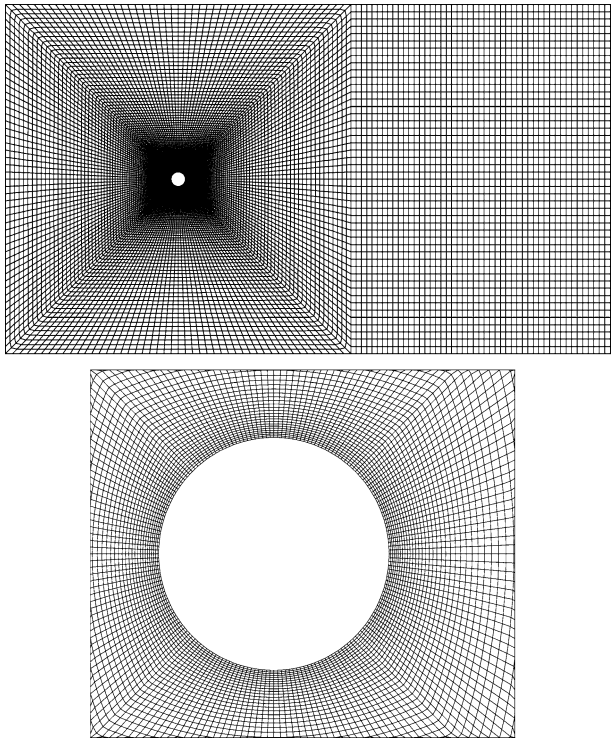

**Fig. 3** Circular cylinder. Numerical grid $G1$ for $Re = 1.4 \times 10^5$

high Reynolds number flow around a square cylinder show that the mean-flow parameters (e.g., Strouhal number and the lift and drag coefficients) are practically insensitive to the levels of turbulence intensity ($T_u \equiv u'/U_o$) in the incident stream provided that $0 < T_u \leq 0.02$. The higher limit was chosen here - a level similar to that obtained in [27]. The turbulent kinetic energy was deduced from the isotropic turbulence relation:

$$k_o = \frac{3}{2}(T_u\, U_o)^2. \tag{18}$$

$\epsilon$ was prescribed by inverting the eddy-viscosity relation (5) and using the Kolmogorov expression for $\epsilon$:

$$\epsilon = C_\mu \frac{k^{\frac{3}{2}}}{L_\epsilon}. \tag{19}$$

According to Bearman and Morel [29], the dissipation scale $L_\epsilon$ is about twice the integral scale $L_x$ and Eq. (19) then gives :

$$\left(\frac{\nu_t}{\nu}\right)_0 \approx 0.22\, T_u\, \mathrm{Re}\left(\frac{L_x}{H}\right)_0. \tag{20}$$

For $L_x/H \approx 1$, the value of $(\nu_t/\nu)_0$ at inlet was 88, which is appropriate for a low intensity turbulent flow.

At outlet, the streamwise gradients of all dependent variables were set equal to zero. Similarly, the normal gradients were set equal to zero at the side planes. At the cylinder walls, integration through the viscous sub-layer directly to the wall was not possible since a high turbulence Reynolds–number model was used. Consequently, the boundary conditions for the velocity components consisted of specifying the momentum fluxes at the wall. These were deduced from a standard logarithmic law of the wall (with $\kappa = 0.41$ and roughness parameter $E = 8.6$). The values of $k$ and $\epsilon$ there were fixed by the assumption of local equilibrium.

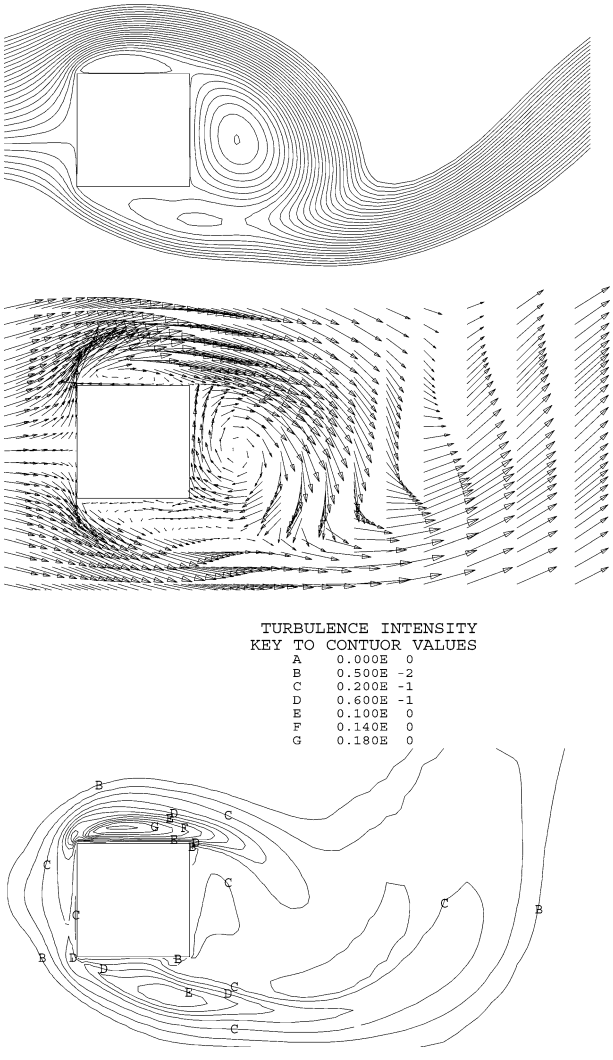


**Fig. 4** Square cylinder. Instantaneous streamlines, velocity vectors and turbulence kinetic energy at maximum $C_L$

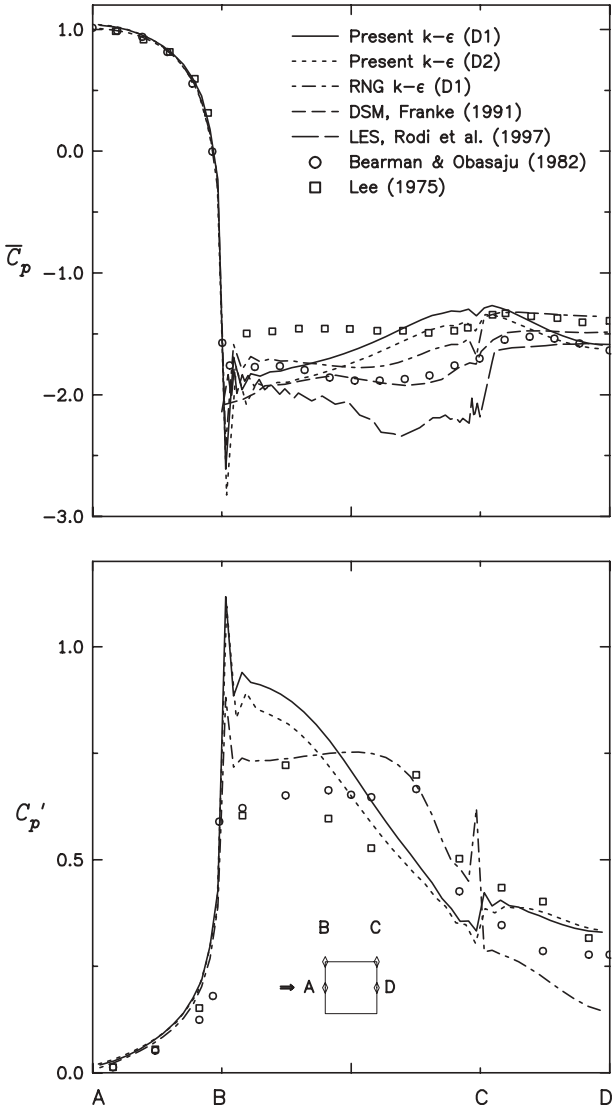


**Fig. 5** Square cylinder (Re = 20000). Predicted and measured mean and r.m.s. values of surface pressure coefficient

**Table 3** Square cylinder. Predictions and measurements of mean-flow parameters

| | St | $\overline{C}_D$ | $C'_D$ | $C'_L$ | $\overline{L}_r/H$ |
|---|---|---|---|---|---|
| Experiments | 0.13–0.139 | 2.16–2.28 | 0.18–0.23 | 1.1–1.4 | 0.88–1.0 |
| Standard $k$-$\epsilon$ | 0.118 | 1.544 | 0.0008 | 0.088 | 2.39 |
| Modified (D1) | 0.141 | 2.199 | 0.186 | 1.386 | 0.65 |
| Modified (D2) | 0.144 | 2.239 | 0.186 | 1.247 | 0.85 |
| RNG | 0.139 | 2.064 | 0.092 | 1.369 | 0.59 |
| Franke [30], DSM-1 | 0.136 | 2.150 | – | – | 0.48 |
| Franke [30], DSM-2 | 0.159 | 2.43 | – | – | 0.48 |
| Rodi et al. [5], LES | 0.130 | 2.300 | 0.140 | 1.150 | 0.96 |

## 4 Results and discussion

### 4.1 Square Cylinder

An overall impression of the flow around a cylinder is presented in Fig. 4 which shows plots of the instantaneous streamlines, the velocity vectors and contours of the turbulent kinetic energy at the phase of the shedding cycle which corresponds to the point where the lift coefficient is at maximum. The mean-flow streamlines and the velocity vectors indicate that, at this phase, the vortex centre is located at $(x, y) \approx (0.9H, -0.1H)$ relative to the centre of the cylinder. The highest levels of turbulence kinetic energy are obtained above the upper side of the cylinder, within the separated shear layer where the velocity gradients are large. Note the reattachement of the separated boundary layer on the top side of the cylinder.

The predicted and measured values of Strouhal number, the mean drag coefficient, the r.m.s. values of the drag and lift coefficients, and the time-mean length of the recirculation region are compared in Table 3. The table also shows the results of Franke [30] obtained with a Differential Stress Model (DSM) using two alternative treatments of the near-wall region. This model will have involved the solution of a total of five differential equations for turbulence quantities. The three-dimensional LES results of Rodi et al. [5] are also included for comparison. Note in that Table the very low values of fluctuations in the lift and drag

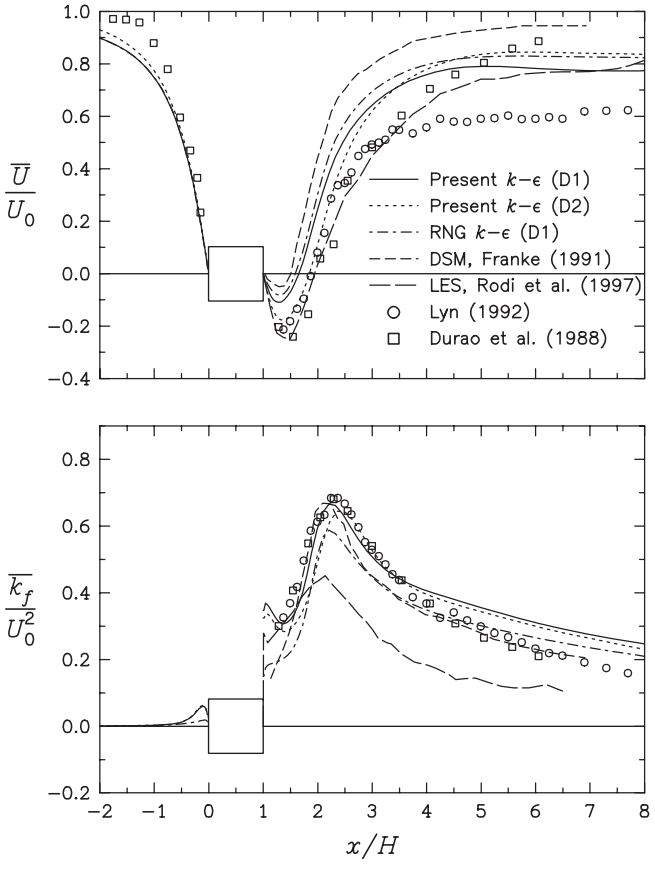


**Fig. 6** Square cylinder. Predicted and measured time-averaged velocity and total fluctuating kinetic energy along the centreline

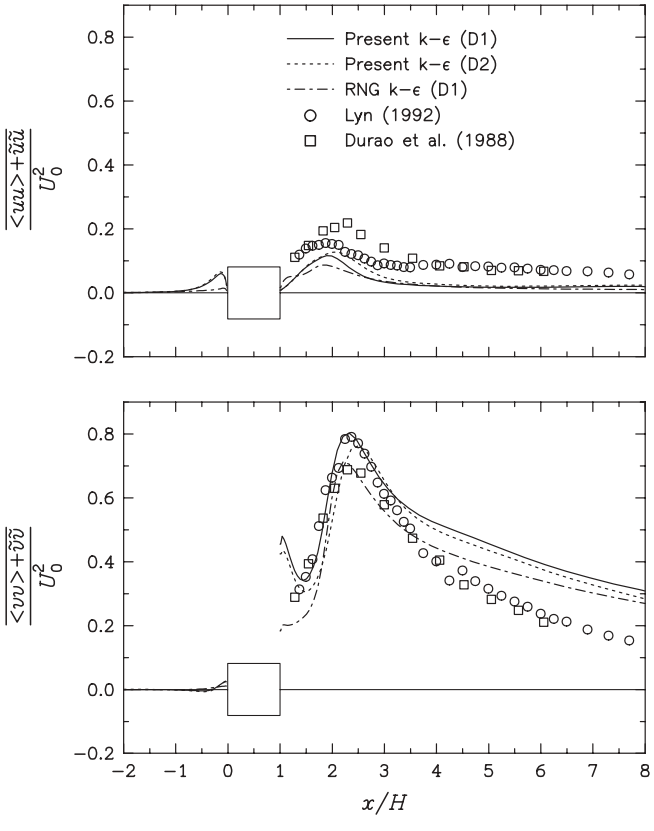


**Fig. 7** Centreline distributions of time-mean apparent normal stresses in streamwise and transverse directions

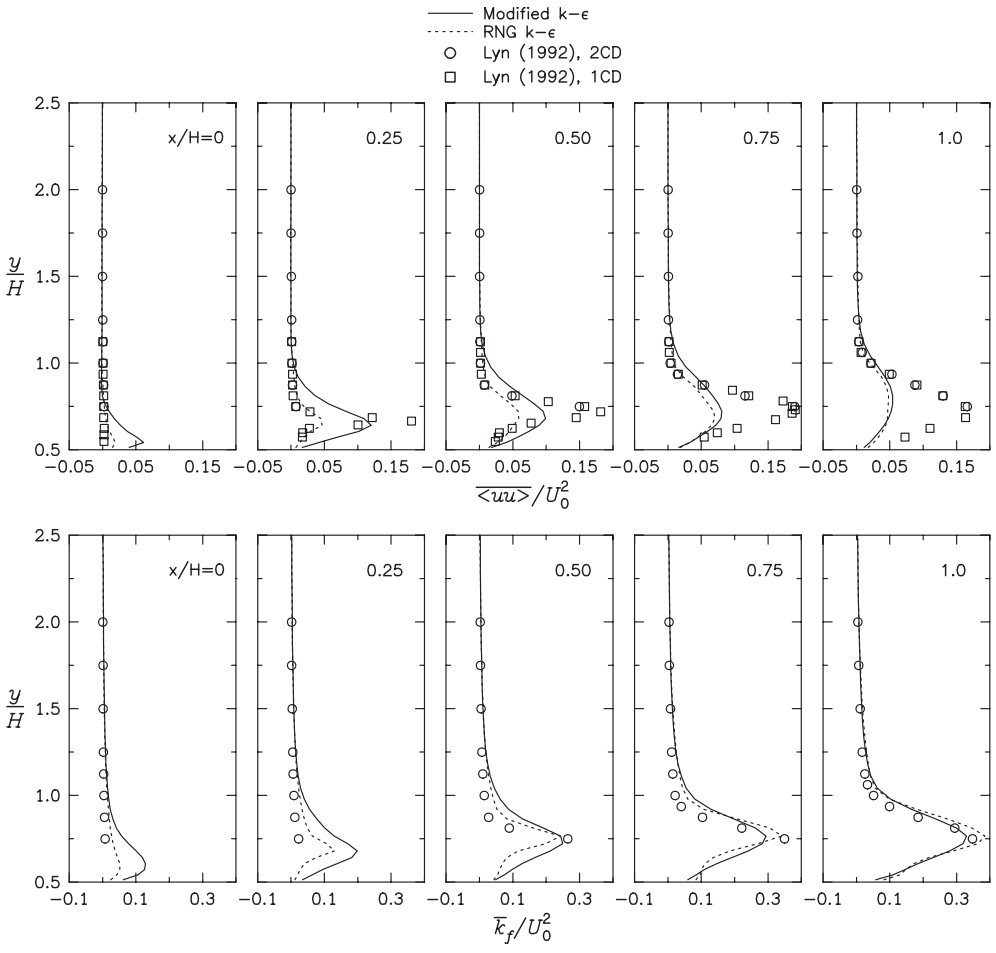


**Fig. 8** Time-averaged profiles of the Reynolds-stress component $\langle u^2 \rangle$, and the fluctuating kinetic energy along upper side of square cylinder

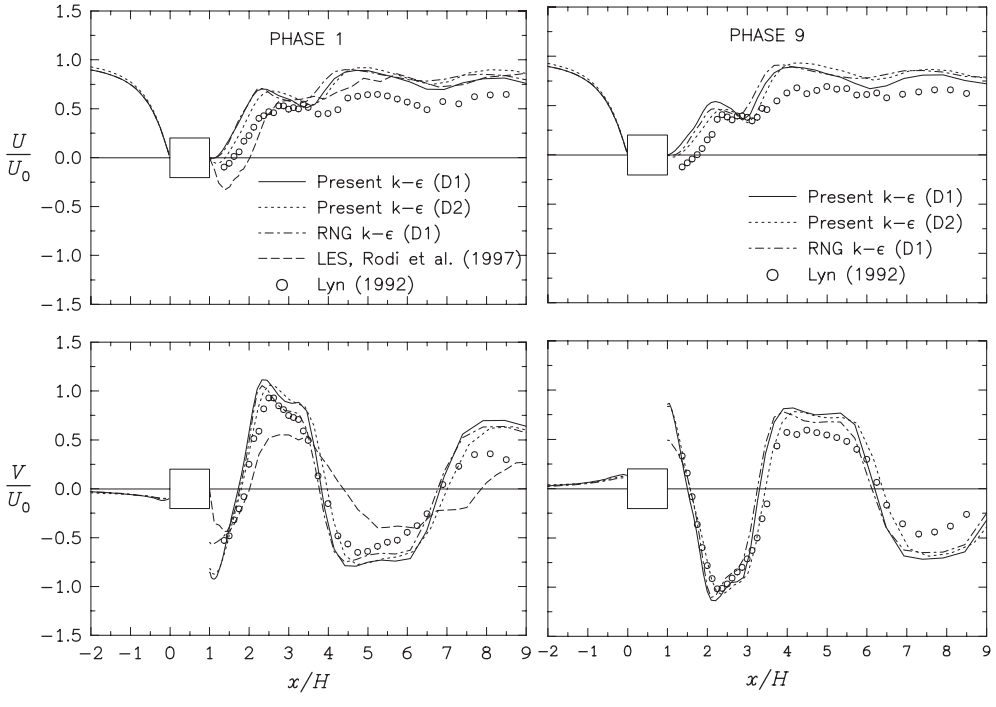


**Fig. 9** Square cylinder. Predicted and measured phase-averaged axial and vertical velocities along centreline

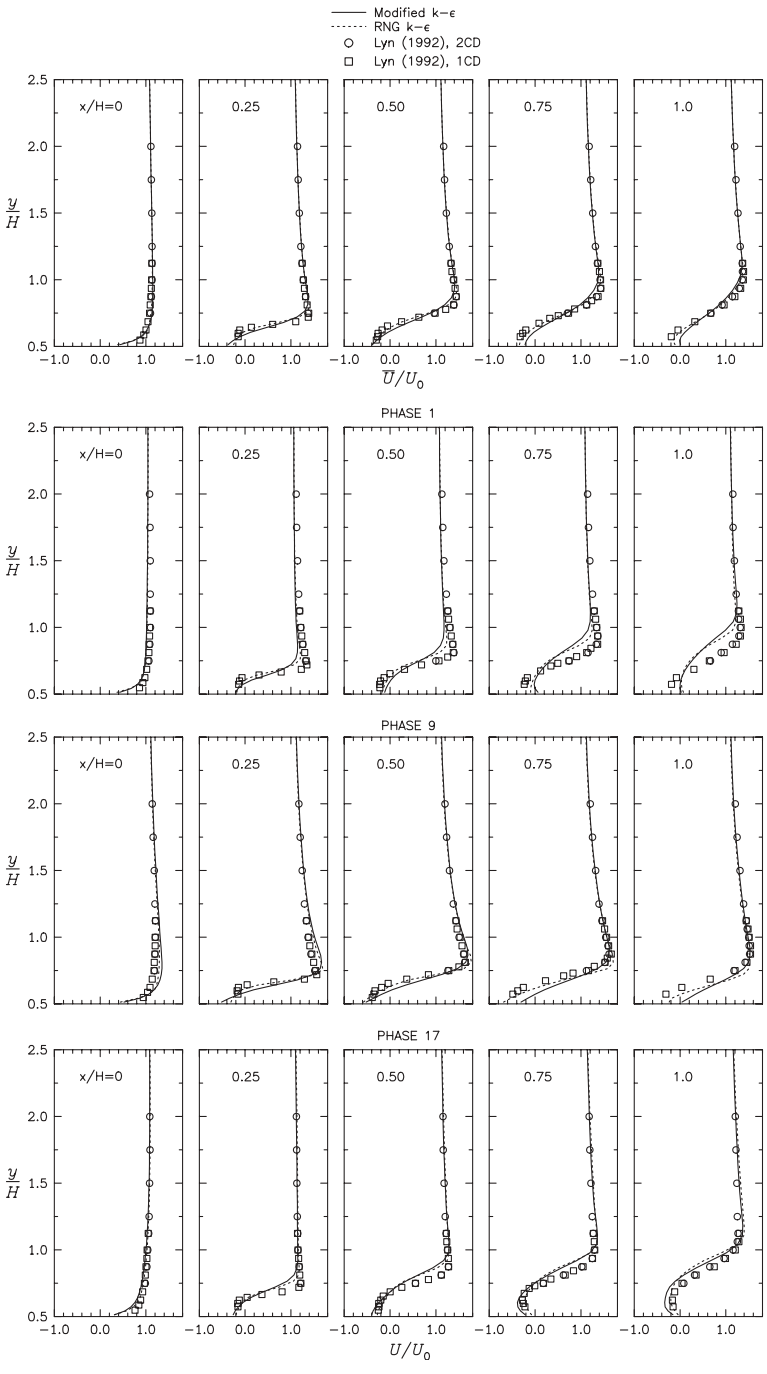


**Fig. 10** Predicted and measured long-time averaged (top) and phase averaged axial velocity profiles along top of square cylinder

coefficients obtained with the standard model. This is the central defect in this model which, interestingly, still manages to obtain a reasonable value for Strouhal number. The modified model of Eq. (15) produces results that are in close agreement with the measurements, especially for the r.m.s. values of $C_L$ and $C_D$. The relative differences between this model's results and the consensus of the experimental values are 5.1, −1.0, −9.3, 10.9, and −25.7% for the Strouhal number, the mean drag coefficient, r.m.s. drag and lift coefficients, and the recirculation zone length, respectively. The RNG model underestimates the mean and r.m.s. values of $C_D$, and the length of the recirculation zone. The length of the recirculation zone depends very strongly on the blockage ratio with $\overline{L}_r = 0.88$ for $B_f = 7\%$ [27], and 1.0 for $B_f = 14\%$ ([14]). The modified model reproduces fairly well the length measured by Lyn when the width of the solution domain is taken to produce a similar blockage ratio. Thus when grid $D2$ is used, the relative difference is −3.9% which compares well with a difference of 9% with the LES results [5]. The DSM-2 model, which utilizes a complicated two-layer near-wall treatment, appears to overestimate $St$ and $C_D$.

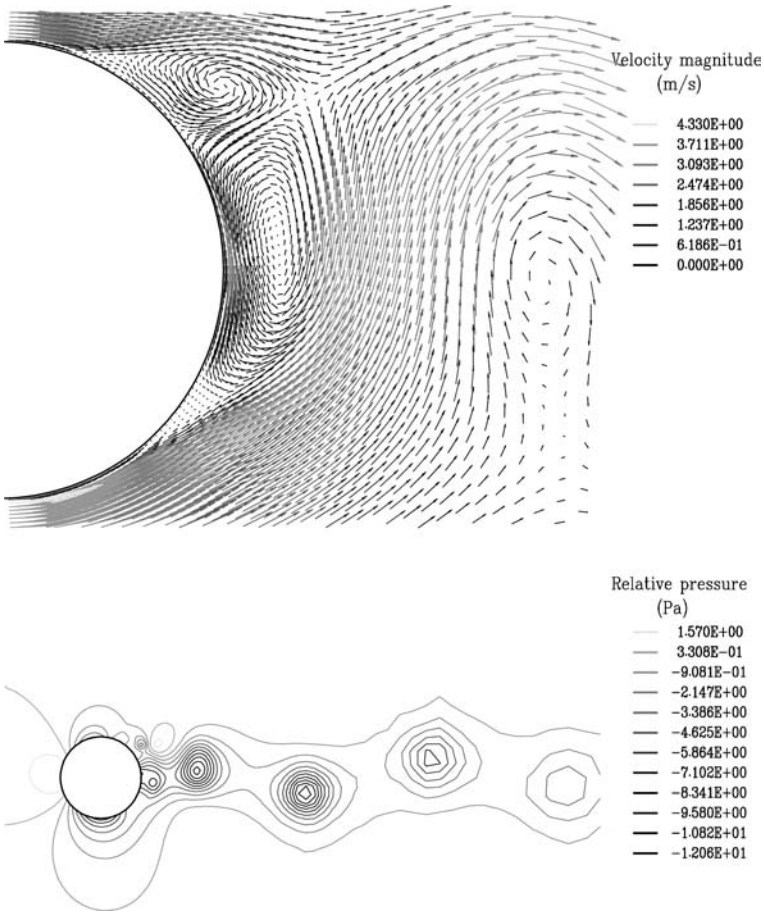


**Fig. 11** Circular cylinder (Re = $1.4 \times 10^5$). Plots of velocity vectors and pressure contours at minimum $C_L$

Attention is now turned to the distributions of the mean and the root-mean-square pressure coefficients on the cylinder's surface. The predicted and measured values are compared in Fig. 5. On the upstream face AB, the mean pressure is predicted quite well by all models but significant differences exist everywhere else. These differences are within the range of experimental uncertainty on the base CD and they are directly related to the variations in the predicted mean drag coefficients observed earlier. Although the modified model predicts fairly well the mean drag coefficient, the result for the mean pressure behind the rear corner C appears to show a faster rate of reduction than is suggested by the data. This is probably a consequence of the continuous pressure increase along the top side BC. The variation on the top face is captured fairly well by the RNG model and less successfully by the DSM model. The LES result seriously underestimates the mean values of surface pressure along the top side. The present predictions of the r.m.s. pressure coefficient are compared with the measured data, Fig. 5. Both the modified and the RNG models predict the r.m.s. values on the upstream and back sides satisfactory though only the RNG model appears to correctly capture the plateau observed on the top side of the cylinder.

Figure 6 is a plot of the time averaged streamwise velocity along the centreline. The size of the recirculation zone downstream of the cylinder is captured quite well by the modified model when grid D2 is used to obtain a similar blockage ratio as in Lyn's experiments. This parameter is also well predicted with the LES method. The influence of the blockage ratio can be seen from the results obtained with the D1 grid, the RNG and the DSM models, all of which significantly underestimate the size of the recirculation zone. Further downstream, the data of Lyn and Durao et al. are significantly at variance with each other and thus it is not possible to determine which model, if any, predicts the correct recovery. The variation of velocity upstream of the stagnation point is also dependent on the blockage ratio as can be seen from the results for the two domains D1 ($B_f = 8.33\%$) and D2 ($B_f = 4.17\%$) and from Durao et al.'s data ($B_f = 14\%$).

The total fluctuating kinetic energy is plotted in Fig. 6. Upstream of the cylinder, the modified model produces what appears to be relatively large levels of this quantity though this does not cause the suppression of vortex shedding. The results with the LES method considerably underestimate the total kinetic energy fluctuations downstream of the cylinder.

The sum of the apparent normal Reynolds stresses defines the fluctuating kinetic energy $k_f$ and it is of interest to show their individual contributions to $k_f$. This is shown in Fig. 7. Both the modified and the RNG models underestimate the axial component of normal

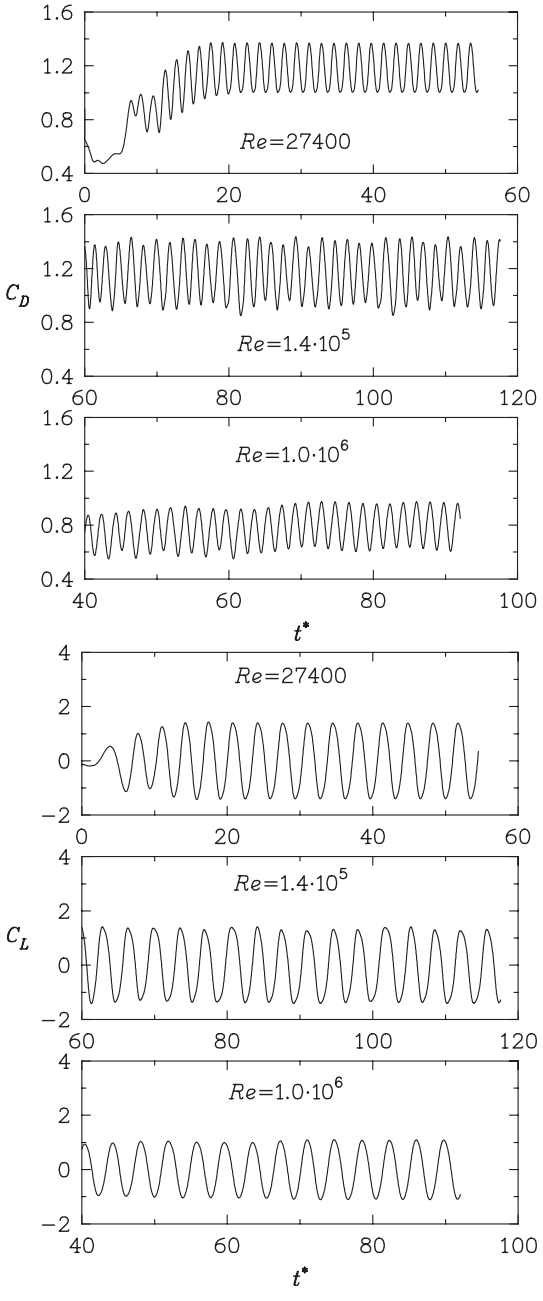


**Fig. 12** Circular cylinder. Time histories of $C_L$ and $C_D$

stress. This turns out in the present flow to be much smaller than the transverse component due, in part, to the enhancement of the latter by the flapping of the shear layer [31]. The modified model captures, fairly accurately, the peak values of the measured transverse component. The results for the two domains D1 and D2 indicate a small dependence of these stresses on the blockage effect though the computed results for the two domains show a shift between the locations of the peak values which is also present in the measurements of the axial normal stresses.

Consideration is now turned to the models' performance in the shear layer region, above the top side of the

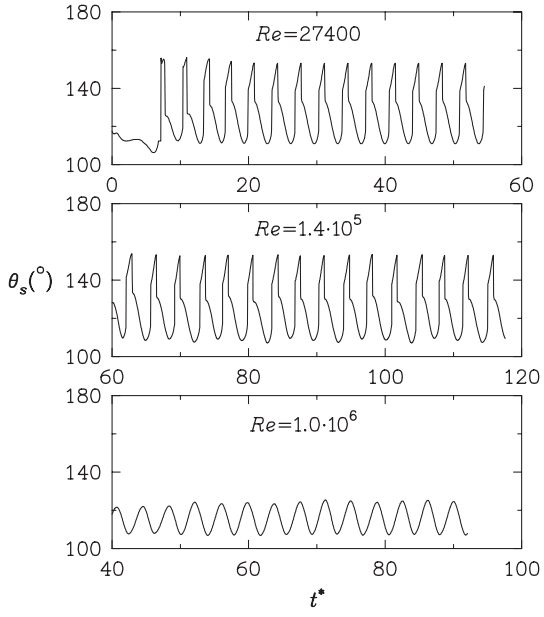


**Fig. 13** Circular cylinder. Time history of angle of flow separation

cylinder, Fig. 8. Plotted there are the results for domain with the smaller blockage ratio D1 and the two sets of measurements reported by Lyn [27]. The evolution of the

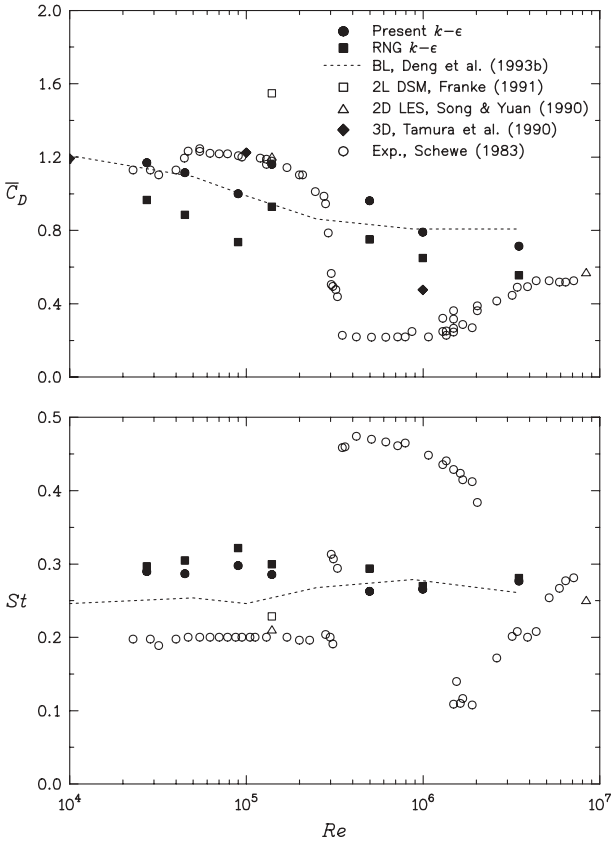


**Fig. 14** Circular cylinder. Computed mean drag coefficient and the Strouhal number

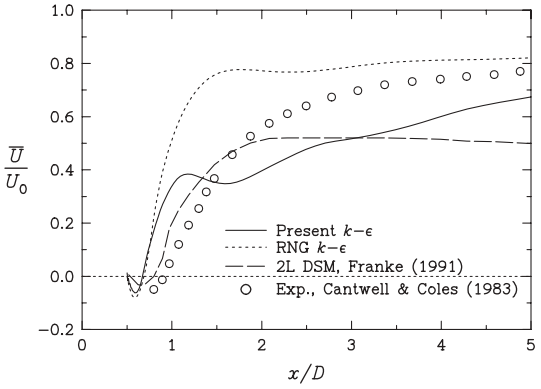


**Fig. 15** Predicted and measured time–averaged centreline velocity for circular cylinder at Re = $1.4 \times 10^5$

normal stresses in the streamwise direction shows that the models do not quite match the high levels found in the experiments with the modified model results being overall the better of the two. The models results along the first half of the face are obviously affected by levels of turbulent fluctuations transported from the stagnation region. As in the wake region, the measured levels of the total fluctuations are captured reasonably well by both models.

Lyn also reported extensive phase-averaged measurements for various parameters and these are used here to check the models. The period of a shedding cycle was deduced in both the measurements and the predictions from values of the static pressure at the mid-point of the top face of the cylinder. The period was then divided into 20 intervals (thus phase 0 corresponds to the beginning of the shedding cycle, phase 1 to $T/20$, and so on) and phase-averaged results obtained for each interval. In the computations, these averages were constructed from results of 17 complete cycles. Figure 9 presents the predicted and measured distributions of the phase-averaged axial and vertical components of velocity along the centreline. The LES results for phase 1 are also shown. These clearly reveal a significant overestimation of the recirculation zone size and underestimation of the peak value of cross-stream velocity

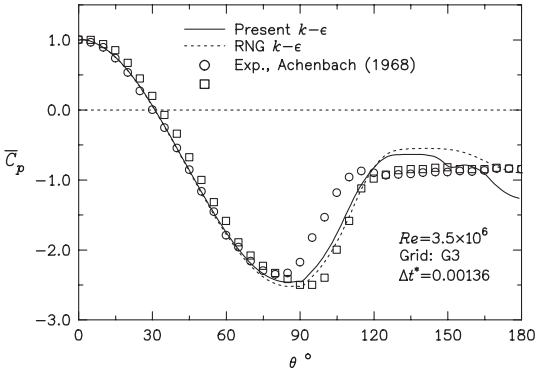


**Fig. 16** Predicted and measured time–averaged wall pressure coefficient for circular cylinder (Re = $3.5 \times 10^6$)

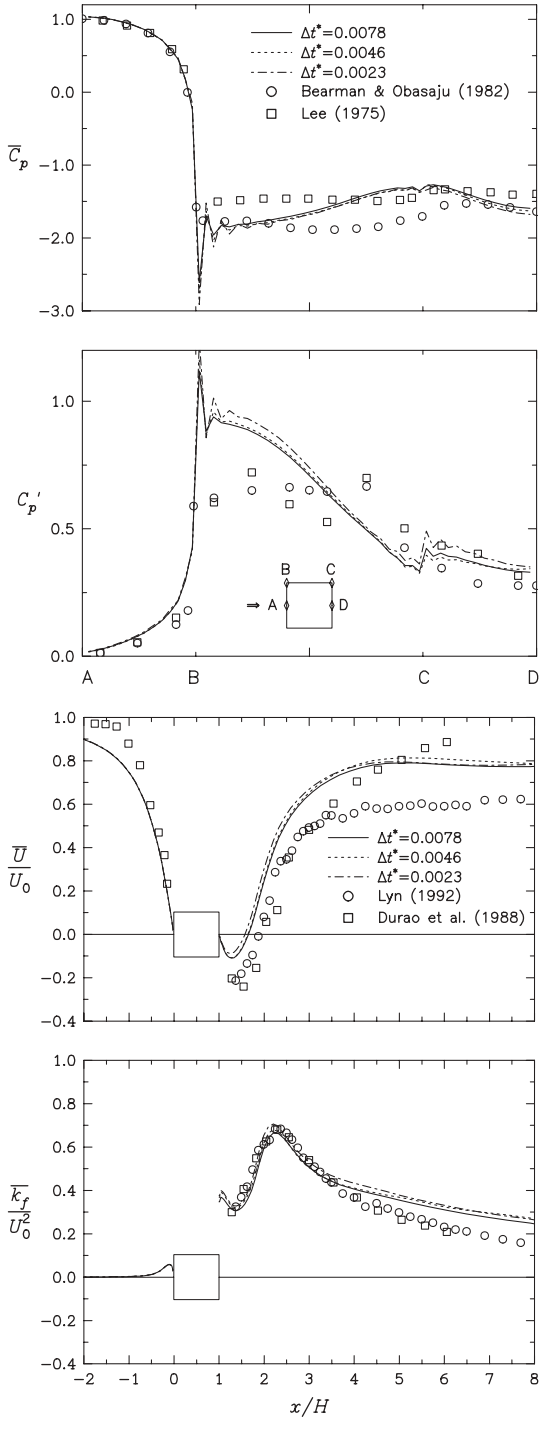


**Fig. 17** Effects of the time-step size on the time-averaged distributions of the pressure coefficient, the streamwise velocity and the fluctuating kinetic energy

downstream of that zone. Figure 10 shows the phase-averaged results for the axial velocity component at five lateral cross-sections along the top cylinder's side and at three phases: 1, 9 and 17. The long-time-averaged profiles are also displayed. Clearly, both the modified and RNG models predict the time-averaged velocity distributions fairly well and manage, to varying degrees of

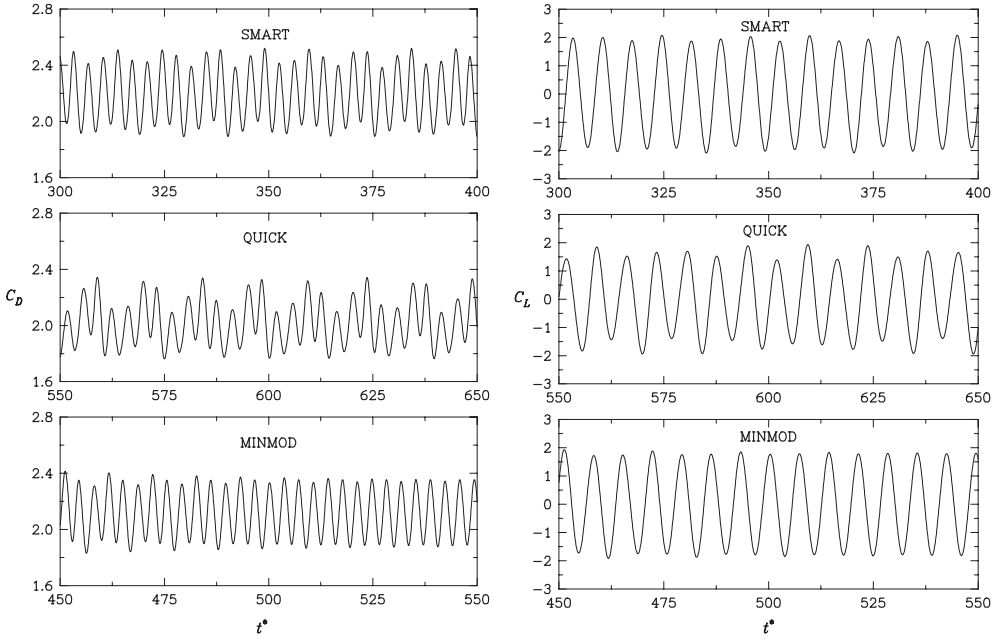


**Fig. 18** Square cylinder (Re = 20,000). Time histories of the drag (left) and lift (right) coefficients as calculated by three different discretisation schemes

success, to reproduce most of the features observed in the measurements. The comparison of the predicted results for the axial velocity component with experiments shows generally reasonable agreement except perhaps in the far wake region.

## 4.2 Circular Cylinder

Predictions were obtained for Reynolds number in the range $2.7 \times 10^4$ – $3.5 \times 10^6$. Table 4 lists the principal parameters for these computations; namely the near–wall distances (expressed as a proportion of $D$), the number of cells in contact with the cylinder surface and the total number of active cells within the flow domain.

An overview of the computed flow field is presented in Fig. 11 which shows details of the flow field in the near wake for $\mathrm{Re} = 1.4 \times 10^5$. These results were obtained with the modified model at the phase of the shedding cycle where $C_L$ is at minimum. The velocity vectors show delayed separation and a significantly narrower wake than was the case for the square cylinder. The pressure contours form a typical pattern that characterizes the vortex shedding process.

The time histories of the force coefficients and the angle of separation are shown in Fig. 12 while that of the separation angle is shown in Fig. 13. Results are presented for three values of *Re*: $2.74 \times 10^4$, $1.4 \times 10^5$ and $1.0 \times 10^6$. The plots show the existence of a well-established periodic vortex shedding process. In the case of subcritical regime ($\mathrm{Re} \leq (3-4) \times 10^5$), the angle of separation varies significantly with the phase, with maximum values of around 155° being attained. In comparison with the experimental values of the flow separation points, the separation is delayed by up to 45° for the subcritical regime. It is fairly well predicted for the postcritical regime ($\mathrm{Re} \geq 10^6$), where data suggest $\overline{\theta}_s \approx 115 - 122°$ [32].

Table 5 summarizes the results for the time-averaged integral parameters as obtained with the modified and the RNG models. Overall, the modified model produces relatively higher values for the force coefficients and

**Table 4** Circular cylinder. Parameters of computational grids used

| Grid | $\Delta n_c/D$ | Cells/ cylinder | Cells | Re |
|---|---|---|---|---|
| *G*0 | $5.75 \times 10^{-3}$ | 160 | 14000 | $2.7 \times 10^4 - 9 \times 10^4$ |
| *G*1 | $3.45 \times 10^{-3}$ | 192 | 20736 | $1.4 \times 10^5$ |
| *G*2 | $1.38 \times 10^{-3}$ | 240 | 31800 | $5.0 \times 10^5$ |
| *G*3 | $5.75 \times 10^{-4}$ | 288 | 45936 | $1.0 \times 10^6$; $3.5 \times 10^6$ |

**Table 5** Turbulent flow around a circular cylinder. Predicted integral parameters using the modified model, and RNG

| Re | $\Delta t^* \times 10^3$ | $Y^+$ | St | $\overline{C}_D$ | $C'_D$ | $C'_L$ | $\overline{\theta}_s(^\circ)$ |
|---|---|---|---|---|---|---|---|
| Modified model | | | | | | | |
| 27 400 | 3.41 | 2–17 | 0.290 | 1.171 | 0.134 | 1.016 | 126.7 |
| 45 000 | 2.80 | 2–28 | 0.287 | 1.117 | 0.115 | 0.999 | 127.7 |
| 90 000 | 2.80 | 10–50 | 0.298 | 1.001 | 0.099 | 0.939 | 130.2 |
| $1.4 \times 10^5$ | 2.18 | 7–42 | 0.286 | 1.162 | 0.178 | 1.006 | 124.1 |
| $5.0 \times 10^5$ | 3.11 | 8–66 | 0.263 | 0.963 | 0.262 | 1.019 | 117.6 |
| $1.0 \times 10^6$ | 1.56 | 5–52 | 0.266 | 0.792 | 0.120 | 0.776 | 115.9 |
| $3.5 \times 10^6$ | 2.72 | 7–176 | 0.277 | 0.715 | 0.103 | 0.743 | 119.6 |
| RNG | | | | | | | |
| 27 400 | 3.41 | 2–18 | 0.297 | 0.967 | 0.094 | 0.926 | 125.1 |
| 45 000 | 2.80 | 2–30 | 0.305 | 0.887 | 0.089 | 0.888 | 127.4 |
| 90 000 | 2.80 | 3–46 | 0.322 | 0.738 | 0.076 | 0.795 | 131.6 |
| $1.4 \times 10^5$ | 1.52 | 3–52 | 0.301 | 0.926 | 0.101 | 0.932 | 125.1 |
| $5.0 \times 10^5$ | 3.11 | 5–68 | 0.294 | 0.753 | 0.071 | 0.740 | 116.6 |
| $1.0 \times 10^6$ | 0.78 | 5–52 | 0.270 | 0.650 | 0.058 | 0.687 | 119.6 |
| $3.5 \times 10^6$ | 1.36 | 3–169 | 0.281 | 0.557 | 0.048 | 0.603 | 122.3 |

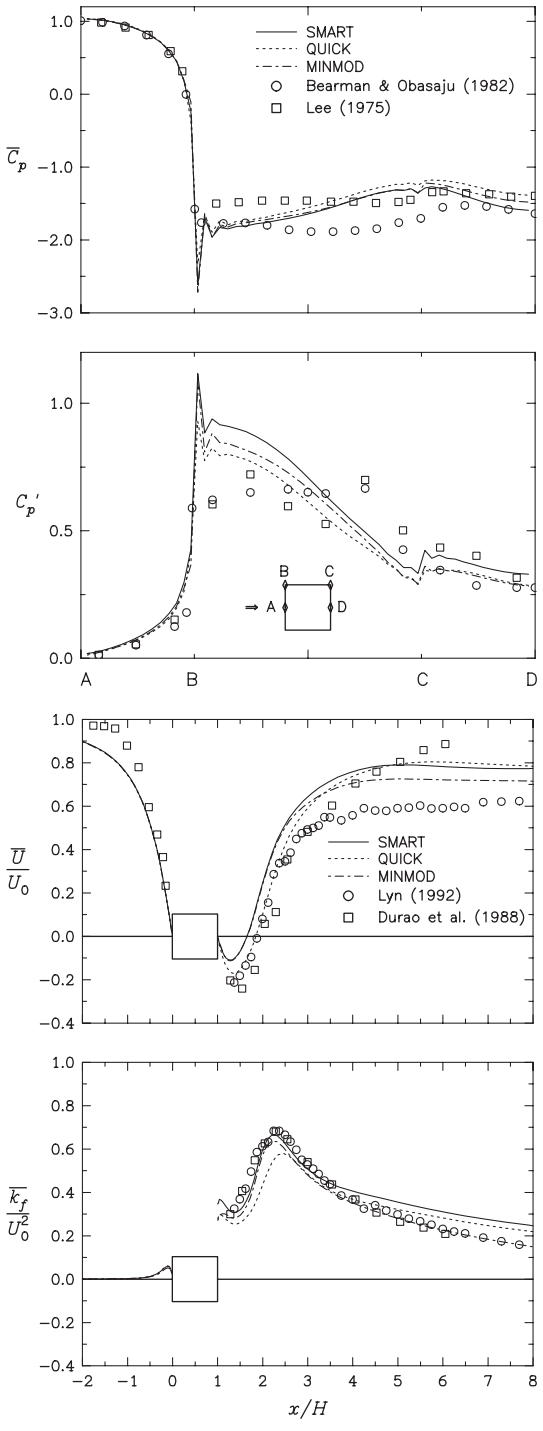


**Fig. 19** Sensitivity to discretisation scheme. Time-averaged pressure coefficients, streamwise velocity and fluctuating kinetic energy

lower values for the Strouhal number, compared to the RNG results. The table also shows the time–step size and the range of $Y^+$ values for the grid nodes closest to the wall. Various tests have shown that the predictions of vortex shedding from circular cylinders are quite sensitive to the location of the near–wall cells. For this reason, it was appropriate to adopt the smallest practical values for $\Delta n_c/D$ even though that meant that, at certain phases of the shedding cycle, the values of $Y^+$ there fell to below the values for which the logarithmic velocity profile can be assumed to apply.

The present results for the variation of the mean drag coefficient and the Strouhal number with Reynolds number are compared in Fig. 14 with the data and with results from other numerical studies. As expected, in the subcritical regime, with the boundary layers remaining laminar up to the separation point, and transition to turbulence occurring in the separated shear layer, the drag coefficient is underpredicted by the present models which assume the flow to be fully turbulent everywhere. The same models also overpredict the drag in the critical regime so that the drag crisis is not reproduced. To do that would require the use of a low Reynolds number model to carry the integration through the viscous sublayer down to the wall and, also, the incorporation of the effects of intermittency on the turbulent stresses [33]. Interestingly, the Strouhal number does not exhibit large variations in the same range of Reynolds number with its value remaining between 0.25 and 0.30.

Figure 15 shows the predicted and the measured time–averaged velocities along the centreline downstream of the cylinder and of the wall static-pressure coefficient at $\mathrm{Re} = 1.4 \times 10^5$. Both the modified and the RNG models produce much shorter recirculation zones than the measurements. Better results were obtained by Franke [30] but only by switching off the turbulence model upstream of the measured separation point. However, downstream recovery is poorly predicted with the same approach.

High turbulence Reynolds-number models are inherently more suited to the postcritical flow regime where the boundary layers become turbulent upstream to the separation points. This expectation is bourne out in Fig. 16 which displays the time–averaged wall pressure coefficient computed by the modified and the RNG models at $\mathrm{Re} = 3.5 \times 10^6$. There is satisfactory agreement with experiments of Achenbach [32] for the same Reynolds number.

## 5 Closure

The central theme of this paper is that turbulence closures fail to predict the correct behaviour of flows dominated by vortex shedding because they fail to capture an essential aspects of the physics of these flows; namely, the occurrence of direct input of kinetic energy from the organized mean-flow fluctuations into the random turbulence motions. That this is important is amply demonstrated in experiments though no account of it has hitherto been included in computational studies. Here, a relatively straightforward proposal is put forward, based on consideration of spectral energy transfer rates. Computations were then performed to check this model for both square and circular cylinders with their very different mechanisms for flow separation. Overall, the results were in accord with the

**Table 6** Square cylinder. Results for three time-step sizes obtained with the $D1$ grid and the SMART scheme

| $\Delta t(s)$ | $\Delta t^* \times 10^3$ | $St$ | $\overline{C}_D$ | $C'_D$ | $C'_L$ | $\overline{C}_L \times 10^3$ | $\overline{L}_r/H$ |
|---|---|---|---|---|---|---|---|
| 0.025 | 7.77 | 0.1414 | 2.199 | 0.186 | 1.386 | −8.0 | 0.654 |
| 0.015 | 4.66 | 0.1435 | 2.226 | 0.201 | 1.398 | −7.9 | 0.644 |
| 0.0075 | 2.33 | 0.1440 | 2.253 | 0.207 | 1.376 | −16.4 | 0.577 |
| $E_{3t}$% | | −2.41 | −3.20 | −13.53 | 0.97 | – | 17.8 |
| $E_{1t}$% | | −0.35 | −1.12 | −2.89 | 1.60 | – | 11.6 |

measurements especially with regards to the r.m.s. values of the lift and drag coefficients. The proposed model is robust and economical, being based on an eddy-viscosity closure. Its extension to transitional flows via incorporation of a model for intermittency is currently in progress and will be reported upon later.

## Appendix: Quantification of numerical uncertainty

All the calculations reported in the Appendix were performed with the modified model. Only the results for square cylinder are presented; the results for the circular cylinder were essentially similar.

### A Temporal resolution

Predictions were obtained with three very different time-step sizes in order to quantify the extent of uncertainty associated with time discretization.
Table 6 lists the time-step sizes, and the associated results for Strouhal number, mean and r.m.s. values of the lift and drag coefficients and the time-averaged length of the recirculation region, $\overline{L}_r$. Strouhal number is clearly the least sensitive parameter to numerical errors. The r.m.s. value of the lift coefficient is perhaps a better indicator of dependence on the time-step and is seen here to first increase and then decrease with reduction in $\Delta t$. A quantitative measure of discretization errors may be obtained via a number of established techniques the simplest of which is based on Richardson extrapolation [35]. The values of the Estimated Fractional Error for the smallest and the largest (reference) time-step sizes, $E_{1t}$ and $E_{3t}$ respectively, are quoted in the Table. These quantities were evaluated as specified in [35] and indicate the extent to which convergence has been attained. Plots of the variation with the time-step size of the time-averaged pressure distribution on the cylinder surface and of the mean velocity and kinetic energy along the centerline are presented in Fig. 17. Apart from slight differences in the distribution of fluctuating pressures, the results for the smaller of the two time steps are virtually identical.

### B Spatial resolution

Extensive testing of discretization schemes in laminar vortex shedding [19] yielded results that support the use of the SMART scheme of [22] which is third-order and bounded. Here, we contrast this scheme's performance with that of two others: MINMOD [34] and QUICK [23]. The grid used was $D1$ and the time-step size was $\Delta t^* = 0.0078$. The time histories of the drag and lift coefficients obtained with these schemes are displayed in Fig. 18. The QUICK scheme, the formally most accurate of the three, shows larger cycle-to-cycle oscillations. The predicted mean-flow parameters are given in Table 7.

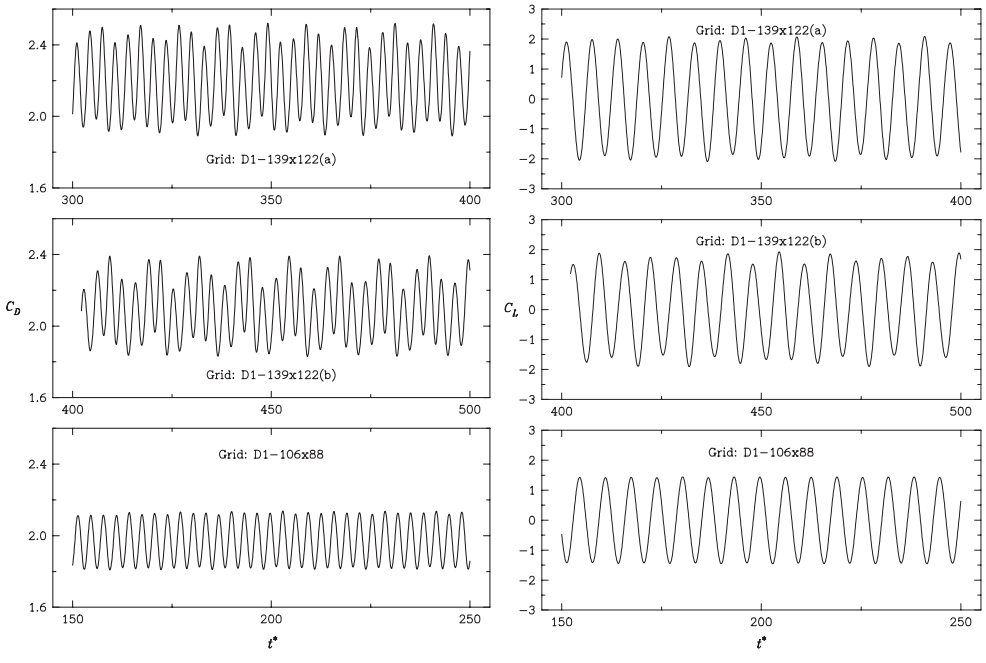


**Fig. 20** Square cylinder (Re = 20000). Time histories of $C_L$ and $C_D$ as obtained with three different grids (SMART scheme and $\Delta t^* = 0.0078$)

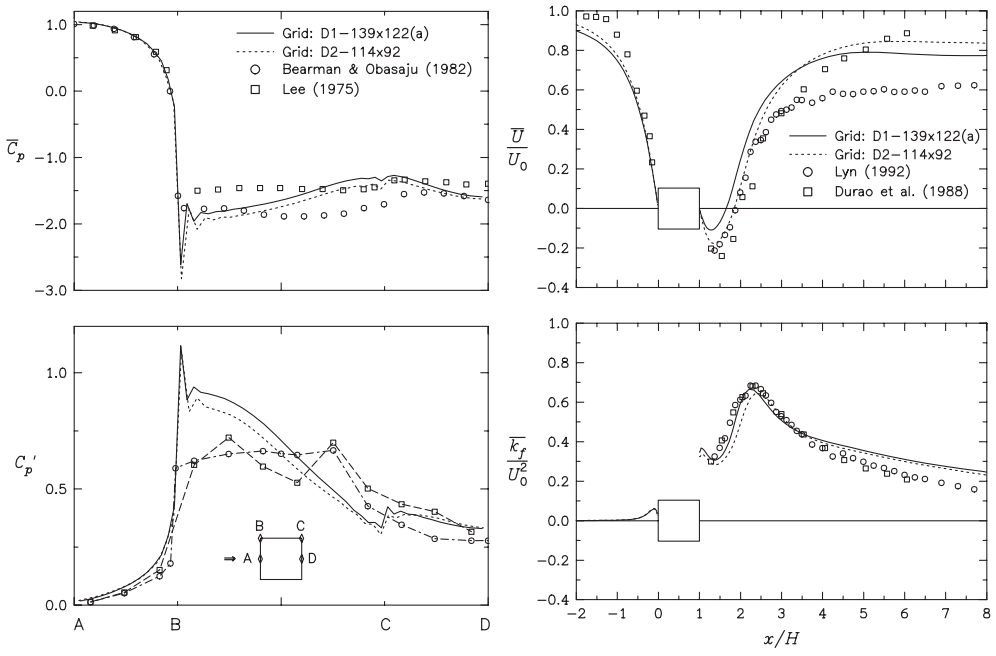


**Fig. 21** Influence of domain size on time-averaged pressure coefficient, streamwise velocity and fluctuating kinetic energy

**Table 7** Square cylinder ($Re = 20000$). Sensitivity to discretisation scheme

| Scheme | St | $\overline{C}_D$ | $C'_D$ | $C'_L$ | $\overline{C}_L \times 10^4$ | $\overline{L}_r/H$ |
|---|---|---|---|---|---|---|
| SMART (S) | 0.1414 | 2.199 | 0.186 | 1.386 | −80 | 0.654 |
| MINMOD (M) | 0.1425 | 2.118 | 0.163 | 1.270 | −2.4 | 0.850 |
| QUICK (Q) | 0.1396 | 2.023 | 0.152 | 1.176 | −5.5 | 0.657 |
| (M−S)/S, % | 0.78 | −3.68 | −12.37 | −8.37 | – | 29.9 |
| (Q−S)/S, % | −1.27 | −8.00 | −18.27 | −15.15 | – | 0.5 |

**Table 8** Square cylinder (Re $= 20000$). Results for various grids obtained by (a) modified and (b) RNG models using $\Delta t^* = 0.0078$ and the SMART scheme

| Grid | St | $\overline{C}_D$ | $C'_D$ | $C'_L$ | $\overline{C}_L \times 10^4$ | $\overline{L}_r/H$ |
|---|---|---|---|---|---|---|
| (a) Modified model | | | | | | |
| D0 − $106 \times 88$ (C) | 0.1412 | 1.972 | 0.110 | 1.009 | −7.9 | 0.912 |
| D1 − $139 \times 122(a)$ (A) | 0.1414 | 2.199 | 0.186 | 1.386 | −80.0 | 0.654 |
| D2 − $139 \times 122(b)$ (B) | 0.1413 | 2.093 | 0.157 | 1.202 | +6.9 | 0.801 |
| (B−A)/A, % | −0.07 | −4.8 | −15.6 | −13.3 | – | 22.5 |
| (C−A)/A, % | −0.14 | −10.3 | −40.9 | −27.2 | – | 39.4 |
| (b) RNG | | | | | | |
| D1 − $139 \times 122(a)$ (A) | 0.1387 | 2.064 | 0.092 | 1.369 | −7.1 | 0.590 |
| D2 − $139 \times 122(b)$ (B) | 0.1207 | 1.722 | 0.082 | 1.048 | −3.2 | 0.540 |
| (B−A)/A, % | −12.98 | −16.6 | −10.9 | −23.45 | – | −8.5 |

**Table 9** Square cylinder. Influence of domain size

| Domain-[Grid size] | $B_f$ (%) | St | $\overline{C}_D$ | $C'_D \times 10^3$ | $C'_L$ | $\overline{C}_L \times 10^4$ | $\overline{L}_r/H$ |
|---|---|---|---|---|---|---|---|
| $D1 - 139 \times 122(a)$ | 4.17 | 0.1414 | 2.199 | 0.186 | 1.386 | 80 | 0.654 |
| $D2 - 114 \times 92$ | 8.33 | 0.1442 | 2.239 | 0.186 | 1.247 | −4.8 | 0.846 |
| (D2−D1)/D1 (%) | | 1.9 | 1.8 | 0.0 | −10.0 | – | 29.4 |

The MINMOD scheme, which is the most diffusive of the three, predicts the highest value for Strouhal number; a similar outcome to what was obtained for the laminar flow cases. The differences between the SMART and QUICK schemes are consistent with the activation of the flux limiters to prevent unboundedness. Figure 19 compares the results for the surface pressure coefficient and the centerline values of mean velocity and kinetic energy as obtained with the different schemes. The absence of very large differences suggest that the results are not too far from being independent of the choice of discretization scheme.

Further tests for grid convergence were performed by obtaining results with three different grids (Table 2). When matching the solutions to the log-law, the cell size in the direction normal to the wall is limited by the non-

dimensional distance $Y^+$ which is constrained not to fall below $\approx 11.6$. Grids $D1-139\times122(a)$ and $D1-139\times122(b)$ have similar expansion factors but different near-wall distances. The coarsest grid $D0-106\times88$ has a greater expansion factor but the same near-wall distances as the grid $D1-139\times122(b)$. The time histories of the drag and lift coefficients, calculated by using these grids are presented in Fig. 20. Table 8 shows the results for the mean-flow parameters where it can again be seen that the Strouhal number is the least sensitive parameter to grid resolution – though not for the RNG model. While the modified model shows acceptable sensitivity to the wall distances, the RNG model yields accurate results only when $Y^+$ is close to the lower limit of $\approx$11.6. The mean value of the drag coefficient obtained with this model is seen to be particularly sensitive to the location of the grid node closest to the wall.

### C Size of solution domain

The placement of the lateral boundaries to the computational domain determines the extent to which blockage effects influence the solutions. To demonstrate the importance of these effects, grids were generated for two domains $D1$ and $D2$, Table 2. The results for the mean-flow parameters are given in Table 12. These were obtained with the SMART scheme, using $\Delta t^* = 0.0078$ and with $\Delta n_c/H = 0.02$. The relative differences between the calculated values are also included. With exception of the r.m.s. lift coefficient, all other predicted parameters increase for the smaller domain $D2$ where the blockage effects are greatest. This trend is also apparent in the distributions of the mean and r.m.s. values of the pressure coefficient shown in Fig. 21.

## References


1. Karniadakis GE, Triantafyllou GS (1992) Three-dimensional dynamics and transition to turbulence in the wake of bluff objects. J Fluid Mech, 238:1–30
2. Zdravkovich MM Flow Around Circular Cylinders, Oxford University Press, Oxford, 1997
3. Jordan SA, Rajab SA (1998) A large eddy simulation of the near wake of a circular cylinder. J Fluids Eng 120:243–252
4. Kravchenko AG, Moin P (2000) Numerical studies of flow over a circular cylinder at Re = 3900. Phys Fluids 12:403–417
5. Rodi W, Ferziger JH, Breuer M, Pourquie M (1997) Status of large eddy simulation: results of a workshop. ASME J Fluids Eng 119:248–62
6. Franke R, Rodi W (1993) Calculation of vortex shedding past a square cylinder with various turbulence models. Turbulent Shear Flows 8, F. Durst et al. (eds.), Springer, New York, pp. 189–204
7. Celik I, Shaffer FD (1995) Long time-averaged solutions of turbulent flow past a circular cylinder. J Wind Eng Indust Aerodynamics 56:185–212
8. Medic G (1999) Etude mathematiques des modeles aux tensions de Reynolds et simulation numerique d'ecoulements turbulents sur parois fixes et mobiles, Ph.D. Thesis. Universite Paris VI, France
9. Younis BA (1988) On modeling vortex Shedding from bluff bodies in laminar and turbulent streams. Proc 7th Int Conf on Offshore Mechanics and Arctic Engineering, Houston, Texas, pp. 23–228
10. Przulj V, Younis BA (1993) Some aspects of the prediction of turbulent vortex shedding. ASME FED, Separated flows 149
11. Kato M, Launder BE (1993) The modelling of turbulent flow around stationary and vibrating square cylinders, 9*th* Symp. on Turbulent Shear Flows, Kyoto, Japan, pp. 10.4.1–10.4.6
12. Younis BA (1999) Prediction of vortex shedding suppression at high Reynolds number. Bull. of the American Physical Society, Ser. II, vol. 44, No. 8
13. Speziale CG (1991) Analytical methods for the development of Reynolds-stress closures in turbulence. Annu Rev Fluid Mech 23:107–157
14. Durao D, Heitor M, Pereira J (1988) Measurements of turbulent and periodic flows around a square cross-section cylinder. Expts Fluids 6:298–304
15. Jung YW, Park SO (2005) Vortex-shedding characteristics in the wake of an oscillating airfoil at low Reynolds number. J Fluids Struct 20:451–464
16. Younis BA, Zhou Y (1997) Accounting for mean-flow unsteadiness in two-equation closures, ICASE report (unpublished)
17. Reynolds WC (1976) Computation of turbulent flows. Annu Rev Fluid Mech 8:183–208
18. Pope SB (2000) Turbulent Flows, Cambridge University Press, Cambridge
19. Przulj V (1998) Computational modeling of vortex shedding flows, Ph. D. Thesis, City University, London, England
20. Yakhot V, Orszag SA, Thangam S, Gatski T, Speziale, C.G. (1992) Development of turbulence models for shear flows by a double expansion technique. Phys Fluids, vol. A4. 1510–1520
21. Younis BA, Teigen P, Przulj VP (2001) Estimating the hydrodynamic forces on a mini TLP with computational fluid dynamics and design-code techniques. Ocean Eng 28:585–602
22. Gaskell PH, Lau AKC (1988) Curvature compensated convective transport: SMART, a new boundedness preserving transport algorithm. Int J Num Meth Fluids 8:617–641
23. Leonard BP (1979) A stable and accurate convective modelling procedure based on quadratic upstream interpolation. Comp Meth Appl Mech Eng 19:59–98
24. Patankar SV, Spalding DB (1972) A calculation procedure for heat, mass and momentum transfer in three-dimensional parabolic flows. Int J Heat Mass Trans 15:1787–1806
25. Lee BE (1975) The effect of turbulence on the surface pressure field of square prism. J Fluid Mech 69:263–282
26. Bearman PW, Obasaju ED (1989) Transverse forces on a circular cylinder oscillating in-line with a steady current. In: Proceedings of the 8th international conference on offshore mechanics and arctic engineering, Hague, March 19–23, pp 253–258
27. Lyn DA (1992) Ensemble-averaged measurements in the turbulent near wake of a square cylinder: a guide to the data, Report CE–HSE–92–6, School of Civil Engineering, Purdue University, USA
28. Gartshore IS (1984) Some effects of upstream turbulence on the unsteady lift forces imposed on prismatic two dimensional bodies. J Fluids Eng 106:419–424
29. Bearman PW, Morel T (1983) Effect of free stream turbulence on the flow around bluff bodies. Prog Aerospace Sci 20:97–123
30. Franke R Numerische Berechnung der instationaren Wirbelablosung hinter zylindrischen Korpern, Ph.D. Thesis, University of Karlsruhe, Germany, 1991
31. Gibson MM, Younis BA (1983) Turbulence measurements in a developing mixing layer with mild destabilising curvature. Expts Fluids 1:23–30
32. Achenbach E (1968) Distribution of Local Pressure and Skin Friction Around a Circular Cylinder in Cross-Flow up to Re = $5\times10^6$. J Fluid Mech 34, Part 4 625–639

33. Younis BA, Berger SA (2004) A turbulence model for pulsatile arterial flows. J Biomech Eng 126:578–584
34. Sweby PK (1984) High resolution schemes using flux limiters for hyperbolic conservation laws. SIAM J Numer Anal 21:995–1011
35. Roache PJ (1994) Perspective: a method for uniform reporting of grid refinement studies. J Fluids Eng 116:405–413